Journal of The
Electrochemical Society

OPEN ACCESS

Evaluation of Gas Bubble Coverage in a Flow Field by Deep Learning-Based Analysis: The Impact of Gas Content on PEM Electrolyzer Performance

To cite this article: Fabian Meyer *et al* 2025 *J. Electrochem. Soc.* **172** 084501

View the article online for updates and enhancements.

You may also like

- A Hybrid Model for Electrokinetic and Stress-Induced Flow Mechanisms in Porous Anodic Oxide Formation
Sajal Wankhede and Dipin S. Pillai
- Electrodeposition of Iridium and Rhenium Layers from Molten Salts and Behavior of Ir/Re-based Coatings under High-Temperature Oxidation Conditions
Andrey V. Isakov, Olga V. Grishenkova and Yuriy P. Zaikov
- Physics-Based Analysis of Cell Imbalances and Aging in Lithium-Ion Battery Modules and Packs
Surya Mitra Ayalasomayajula, Yuliya Preger, Jacob Mueller et al.

ECC-Opto-10 Optical Battery Test Cell:
Visualize the Processes Inside Your Battery!

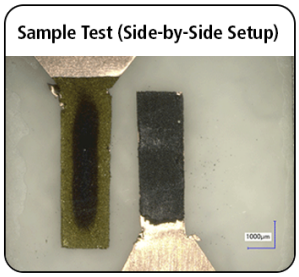
EL-CELL®
electrochemical test equipment

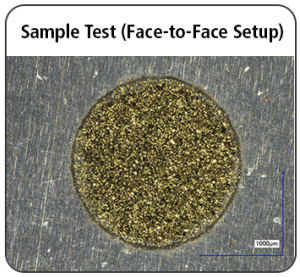
- Battery Test Cell for Optical Characterization
Designed for light microscopy, Raman spectroscopy and XRD.
- Optimized, Low Profile Cell Design (Device Height 21.5 mm)
Low cell height for high compatibility, fits on standard samples stages.
- High Cycling Stability and Easy Handling
Dedicated sample holders for different electrode arrangements included!
- Cell Lids with Different Openings and Window Materials Available



Scan me!

Contact us:
+49 40 79012-734
sales@el-cell.com
www.el-cell.com





This content was downloaded from IP address 134.130.130.178 on 22/10/2025 at 14:00

Journal of The Electrochemical Society, 2025 **172** 084501

Evaluation of Gas Bubble Coverage in a Flow Field by Deep Learning-Based Analysis: The Impact of Gas Content on PEM Electrolyzer Performance

Fabian Meyer,[1,2,z] Violeta Karyofylli,[1] André Colliard Granero,[3] Christoph König,[1] Ali Javed,[1] Michael Eikerling,[3,4] Hans Kungl,[1] Eva Jodat,[1] André Karl,[1] and Rüdiger-A. Eichel[1,2,5]

[1]*Fundamental Electrochemistry (IET-1), Forschungszentrum Jülich, 52425 Jülich, Germany*
[2]*Institute of Physical Chemistry, RWTH Aachen University, 52074 Aachen, Germany*
[3]*Theory and Computation of Energy Materials (IET-3), Forschungszentrum Jülich, 52425 Jülich, Germany*
[4]*Chair of Theory and Computation of Energy Materials, Faculty of Georesources and Materials Engineering, RWTH Aachen University, 52072 Aachen, Germany*
[5]*Faculty of Mechanical Engineering, RWTH Aachen University, 52062 Aachen, Germany*

Oxygen gas generated at the anode of PEM electrolyzers turns the flow in the anodic flow field into two-phase regime. Along with upscaling the electrolyzers and the objective to reach higher current densities, the impact of the two-phase flow regime becomes an issue of major concern for their future design and operating conditions. To observe and quantify gas bubble formation and local gas content in the flow field channels during operation using a high-speed camera, a test rig for a 25 cm^2 scaled laboratory electrolyzer cell with a transparent flow field has been set up. Current-voltage curves were recorded, while monitoring at the same time the impedance and the gas evolution in the anode flow field. Gas bubbles were distinguished by a deep learning-based image processing algorithm, revealing enhanced gas area coverage and bubble size with increasing current density. Corresponding calculations from a two-phase flow mixture model show a similar trend for local gas content in the flow field. In the high current density region, a strongly increasing voltage along with changes in the impedance pattern coincide with the transition from the flow regime with individual gas bubbles to an interconnected gas flow regime in the majority of the cell.
© 2025 The Author(s). Published on behalf of The Electrochemical Society by IOP Publishing Limited. This is an open access article distributed under the terms of the Creative Commons Attribution 4.0 License (CC BY, https://creativecommons.org/licenses/by/4.0/), which permits unrestricted reuse of the work in any medium, provided the original work is properly cited. [DOI: 10.1149/1945-7111/adf30c]

Manuscript submitted March 27, 2025; revised manuscript received July 3, 2025. Published August 4, 2025.

Supplementary material for this article is available online

Green hydrogen produced by electrolysis with renewably generated power is posed to play a vital role not only in industrial applications such as in fertilizer production or steel manufacturing but also potentially as a key energy carrier and storage medium. To ramp up the green hydrogen production, proton exchange membrane (PEM) water electrolysis is one of the most promising technologies.[1] It can be operated at high current densities, offers high product gas purity and is compatible with dynamic operation profiles which is vitally important when coupled with intermittent power generation from solar or wind.[2–5] On-going developments of PEM electrolysis cells (PEMEC) aim to improve the electrochemical performance and enhance the operational life by applying even higher current densities and further increasing the active area of the electrolytic cell.[6,7] As water is split into gaseous oxygen and hydrogen during the electrolysis process, gas molecules form nuclei from the supersaturated solution, primarily in the pores of the catalyst layer (CL), and grow into bubbles over time that detach when they exceed a certain detachment radius.[8,9] Then the detached bubbles are transported through the porous transport layer (PTL), which also ensures efficient water supply and electron conduction, from the catalyst layer into the flow field, resulting in a two-phase flow of liquid water and gaseous oxygen in anodic flow fields and a two-phase flow of liquid water and gaseous hydrogen in cathodic flow fields.[10] However, these flow phenomena affect the performance, efficiency, and degradation of PEMEC systems, especially at higher current densities since the formation and transport of gas bubbles can hinder water access to the CL and reduce the active electrode surface by occupying pores within the CL.[8] To ensure effective mass transport in PEMECs, the dynamics of bubble formation and the related flow phenomena must be thoroughly investigated.[9,11–17] For this purpose, transparent cell designs have been used in previous studies, and bubble formation has been analyzed using high-speed video recordings.

In microscopic experimental investigations, bubble formation is directly observed inside the pores of the PTL. In some cases, the pore size is enlarged to an extent that the bubble formation can be observed directly on the electrode surface. For this purpose, titanium meshes with a corresponding mesh width are selected to ensure direct visibility of the electrode. Typically, two distinct types of mobile bubbles were found in these investigations: those that detach and float freely in the water, and those that coalesce with neighboring bubbles and cover the entire pore. In addition, bubbles were observed, which remain stagnant throughout operation.[10,18] These differ optically from the moving bubbles by their bright and dotted surface.[19] Observations with mesh PTLs showed no significant changes of bubble detachment radius with flow rates, whereas observations with felt PTLs indicated a slight decrease of the bubble detachment radius with increasing flow rates. Simultaneously, the detachment radius increases with pore size and increasing current density.[17,20] Investigations with a novel thin tunable PTL with regular and straight-through pores demonstrated that the detachment radius has an influence on the performance. An increase in performance was observed, as indicated by a decreased overpotential directly correlated to the bubble detachment radii being six times smaller compared to the felt PTL.[21]

The phases in the life cycle of bubbles include nucleation, growth, coalescence, wall adhesion and detachment. These were simulated using a volume-of-fluid (VOF) model, which considers the anode side PTL contact angles. This showed a dependency on the flow velocity of the water, resulting in different bubble removal rates in the individual sub-channels.[22] Another pseudo coupled VOF model considering both temperature dependence and current density compares the two-phase flow in a serpentine flow field to that in a parallel flow field. The results show that the serpentine flow field offers a more uniform water supply and better heat removal capacity, but the parallel flow field enables better oxygen removal and thus

[z]E-mail: fa.meyer@fz-juelich.de

results in a more uniform distribution of the current density.[23] The comparison of a flow field with five serpentine channels with a parallel flow field in a transient model substantiates this result.[24] The local current density changes where oxygen accumulates at the interface of PTL and CL. Specifically, at high current densities, regions with oxygen accumulation have a higher overpotential. At lower current densities, gas removal is facilitated while it more readily accumulates at higher current densities.[24]

Experimental studies on the macroscopic observation of the entire flow field covering a range up to 2 $A{\cdot}cm^{-2}$ show a clear trend with increasing current density. The higher the current density, the more gas is produced and a change from bubbly to slug flow occurs.[3,17,18,25–28] One study investigating the two-phase flow at higher current densities up to 3.3 A cm^{-2} compared serpentine and parallel flow fields. Different flow rates and temperatures were investigated in a 9 cm^2 PEMEC, showing that the slug length decreases with an increasing flow rate. Similar to the aforementioned modeling studies, the parallel flow field shows a better performance, especially at high current densities. A correlation between slug length and channel length was observed with slugs being shorter in the parallel flow field compared to the serpentine flow field.[3] The qualitative investigation of the two-phase flow in a 9 cm^2 PEMEC with a parallel flow field evinced at higher current densities gas accumulation in the upper end of the channel, which caused a bubble blockage. The number of stagnant bubbles rises with increasing current density.[18] When vibrations are applied to a transparent PEMEC, the overpotential is lowered leading to an increase in performance. As indicated by the corresponding video recordings, larger bubbles can be split into smaller bubbles by a combination of a suitable flow rate, vibration amplitude and frequency.[25]

An investigation of a 27 cm^2 cell showed a strong influence of temperature, current density and flow rate on the flow regime.[29] Flow types include bubbly flow, for which gas bubbles are smaller than the flow channel width, slug flow (also known as Taylor flow), for which gas bubbles are as large as the flow channel width, churn flow, for which turbulent gas causes bubble slugs to break apart, and ring flow, for which liquid flows as a thin film along the walls and gas as a continuous phase in the middle of the flow channel.[29,30] If the flow rate is increased, a comparatively higher proportion of bubbly flow can be observed.[26] The impact of various water flow rates was also investigated on a 28 cm^2 round PEMEC by applying current densities up to 1 $A{\cdot}cm^{-2}$. Electrochemical impedance spectroscopy (EIS) measurements were carried out in addition to a qualitative video analysis. The bubble size and coverage increased with increasing current density and decreased with increasing flow rate. Simultaneously, the EIS measurements revealed smaller semicircles with increasing current density, which can be attributed to a faster oxygen evolution reaction (OER), as this occurs faster with increasing overpotential.[28]

Investigations of a segmented unit cell of a PEMEC stack under dehydration conditions showed locally heterogeneous voltage, current density and temperature distributions at different stoichiometric water ratios. Local EIS measurements demonstrated an increase in impedance in the areas affected by dehydration.[31] In investigations using a 50 cm long single-channel cell at medium and low flow rates, local EIS measurements as well as performance and current density distributions also reported such dehydration effects, in this case caused by low flow rates, indicated by an increase in impedance and decrease in the performance especially in areas close to the outlet.[32]

All these investigations show a strong dependence of the bubble dynamics and the two-phase flow on the applied current density. However, a detailed connection between electrochemical measurements such as polarization curves and EIS measurements and the video data has not been established yet, or only for low current densities of up to 1 $A{\cdot}cm^{-2}$. There is currently a lack of further investigations for high current densities, which are especially relevant for commercial PEMEC operation. To fill this gap, a transparent PEMEC with an active area of 25 cm^2 was operated up to 3.5 $A{\cdot}cm^{-2}$ in this work. A low flow rate of 3 ml min^{-1} was chosen during the whole operation so that a low stoichiometric ratio ($\lambda = 6$) is present at maximum current density 3.5 $A{\cdot}cm^{-2}$ and the effects resulting from insufficient water supply can therefore be observed. Besides recording polarization curves, detailed EIS measurements were carried out in 0.1 $A{\cdot}cm^{-2}$ steps and video recordings were made of the flow on the anodic side. Using a novel deep learning-based algorithm, video data were quantitatively evaluated and correlated with polarization curves and EIS measurements. In addition, two-phase flow simulations based on the mixture model were performed and compared with the experimental data using the frequency distributions of the gas bubbles in the flow field.

Experimental

Cell setup.—The transparent PEMEC setup was custom-designed and manufactured in-house. The main components of the 25 cm^2 PEMEC device, including the transparent flow fields, current collectors, heating elements, porous transport layers (PTLs), and the membrane electrode assembly (MEA), are shown in Fig. 1. The flow field was directly machined into the end plate made of transparent polymethylmethacrylate (PMMA). The flow field consists of 11 channels aligned in parallel with a length of 44 mm, a width of 3 mm, and a height of 2 mm. Channels perpendicular to these flow channels distribute and collect the inflow/outflow to/from these flow field channels. An electrical connection to the PTLs was provided by

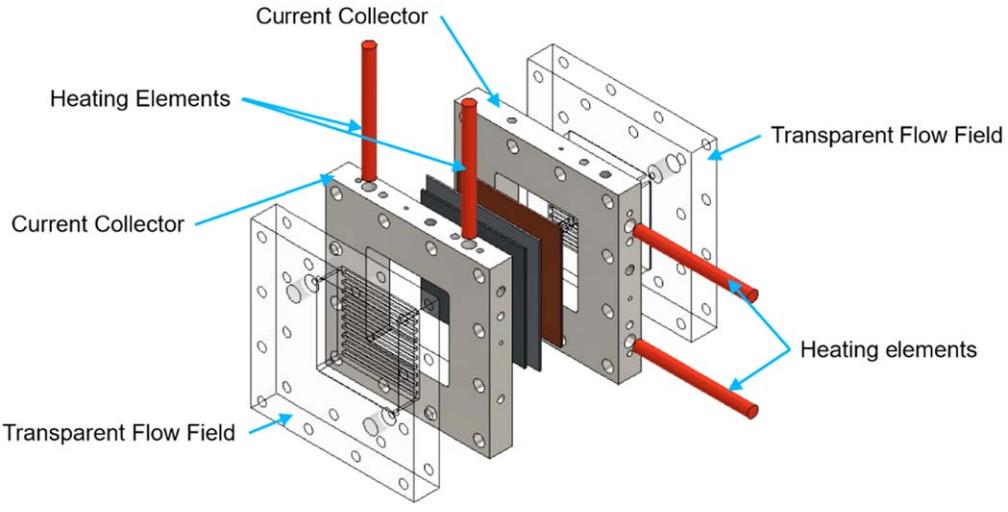


Figure 1. In-house-built transparent PEMEC with integrated active heating.

titanium current collectors in direct contact with the PTL. The current collectors were coated with platinum on the anode side and gold on the cathode side, each with a coating thickness of 2.5 μm. Two heating elements and one thermocouple were integrated into each current collector to actively control the temperature in the PEMEC.

The PTL on the anode consists of two different titanium meshes with mesh sizes of 80 and 18 and wire diameters of 0.13 and 0.28 mm. Both meshes were sputter coated with 100 nm platinum. As the cathode side PTL, two Toray carbon papers (TGP-H-60) and an additional gold mesh for better current distribution were used. As MEAs, HYDRion^{TM} N115 from Ion Power GmbH were used with an anode-side loading of 1 mg Ir/cm^2 and a cathode-side loading of 0.3 mg Pt/cm^2. To ensure cell tightness, silicone-based gaskets with a thickness of 0.8 mm between the flow field and current collector, and with a thickness of 0.6 mm between the membrane and current collector, were inserted. The full cell was assembled using twelve M5 screws with an applied torque of 5 Nm to ensure good contact between the individual components.

Test rig.—The schematic diagram of the test rig is shown in Fig. S1. The electrochemical measurements, including current density-voltage (j-V) curve and EIS, were conducted with a VMP 300 potentiostat from Biologic. The potentiostat has one measurement channel along with 15 booster cards, where each can supply 10 A, so that current densities up to 6 A·cm^{-2} can be realized.

Separate water circuits supply the anode and cathode sides of the PEMEC with deionized (DI) water, with a conductivity of 0.055 μS. The water is circulated throughout the whole experiment with a constant flow rate of 3 ml min^{-1} between the PEMEC and the heated gas/liquid separators via a peristaltic pump from Masterflex SE with two Easy Load II pump heads, which leads to a high stoichiometric ratio at low current densities ($\lambda = 211$ at 0.1 A·cm^{-2}) and low stoichiometric ratio at high current densities ($\lambda = 6$ at 3.5 A·cm^{-2}) as shown in Fig. S2. To control the temperature, SA-88–2k controllers from Pohltechnic.com GbR were used.

PT100 sensors were used to measure the temperatures in the inlet, the outlet and the middle of the flow field for both the anode and cathode sides of the PEMEC. To observe the two-phase flow inside the anode flow field, a high-speed camera from Photron (Fastcam Nova R5 NV) with a set resolution of 2048 × 2048 pixels and a frame rate of 200 fps was used. A macro lens with double magnification was applied to observe the entire flow field. In addition, two LED lights (VD7000-LP) with max. 7280 lumen were used to provide better illumination of the anode flow field view.

Description of image processing algorithm.—A deep learning-based tool developed by Colliard-Granero et al. was implemented to analyze the data from the recorded videos.[33] This deep learning model was trained to detect gas bubbles within the flow field using a custom U-Net architecture with a ResNeXt101 backbone pre-trained on the ImageNet dataset.[34–36] The original images were binarized into black and white images so that the white areas representing the bubbles could be clearly distinguished from other structures such as channels, fluid and boundaries. The model had to be adapted to our dataset before it could autonomously predict gas bubbles in our samples. To achieve this, 50 individual images were manually annotated using the program Label Studio to create the corresponding binary masks.[37] These annotated images, along with the original images, were resized to 512 × 512 pixels to optimize the performance of the model, while avoiding any resolution-related issues. The resized dataset was used to train the algorithm for 200 epochs with a batch size of 8 and a dynamic learning rate that was adjusted based on the model's performance throughout training. Eventually, the resulting model was able to independently identify the gas bubbles and thus autonomously generate black and white predictions on unseen examples.

The model's predicted videos were then used to calculate various parameters using computer vision algorithms. The tool was used to calculate average bubble size, gas coverage and the frequency distribution of gas bubbles. To calculate the average bubble size, the size of each individual bubble in each frame was determined and then the average size per frame was calculated. Each recorded video consists of 2,670 individual frames; the average bubble size per video was obtained by averaging the bubble sizes across all frames. For gas coverage, the sum of all bubble areas per frame was determined and divided by the total channel area, as only the gas bubbles occurring in the channels are relevant to this investigation. To generate the frequency distribution plot, all binary images were overlaid to generate a heat map of the bubble probability density over time. Positions with a higher probability of encountering bubbles were given a red color, while less frequent zones were given cooler colors.

Measurement procedure.—Preceding the experiments for recording the polarization curve (j-V curve), the observation of the gas bubbles in the two-phase flow and the EIS a current density of 1 A·cm^{-2} was applied for one hour. The current density was then reduced to 0.005 A·cm^{-2} and held for 5 min. Then the current density was increased step-by-step. Starting at 0.025 A·cm^{-2}, the current density was increased to 0.2 A·cm^{-2} in 0.025 A cm^{-2} steps. Up to 0.5 A·cm^{-2}, the step size was 0.05 A·cm^{-2}, and then the current density was increased in 0.1 A·cm^{-2} steps up to 3.5 A·cm^{-2}. Data for the polarization curve and EIS spectra are collected over a current density range of 0.1 A·cm^{-2} to 3.5 A·cm^{-2} in increments of 0.1 A·cm^{-2}, with a dwell time of 390 s at each current level, while videos of the two-phase flow in the anode side flow field were recorded. The procedure is illustrated in Fig. S3. The video recording starts five seconds after the corresponding current density was applied. The duration of the video recording is 12 s and was carried out at a set frame rate of 200 fps. To create the polarization curve, the used data points were measured 54 to 60 s after the current density was set. The average value was calculated from these six data points. After that, the current density has been held for 60 s, then the galvanostatic EIS measurement begins. For all EIS measurements a 10% amplitude of the applied current density and a frequency range from 500 kHz to 50 mHz with 5 points per decade and 4 average measurements per frequency were used. After finishing the galvanostatic EIS measurement, the change to the next higher current density was performed.

The impedance measurements were evaluated using an equivalent circuit encompassing a resistor (R_0) connected in series with two different networks; R_1//CPE_1 and R_2//CPE_2, each comprising of a resistor and a constant phase element connected in parallel with each other. The corresponding equivalent electrical circuit diagram is shown in Fig. S4.

Modeling.—The approach to calculating the local and overall gas content inside the flow field at the anode side is based on a 3D two-phase flow mixture model. Several models exist for the simulation of multi-/two-phase flows, and their advantages and disadvantages have previously been delineated.[38] The model choice for this study is further justified in the supporting information (SI).

The computational domain is presented in Fig. S5. The oxygen production and water consumption are introduced via a flux boundary condition (BC) at the PTL surface, which is in contact with the anode catalyst layer. The fluxes of produced oxygen, $\dot{V}_{O_2}\cdot\boldsymbol{n}$, and consumed water, $\dot{V}_{H_2O}\cdot\boldsymbol{n}$, are calculated using Faraday's law as follows:

$$\dot{V}_{O_2}\cdot\boldsymbol{n} = \frac{M_{O_2} j A_{active}}{4F\rho_{O_2}}$$

$$\dot{V}_{H_2O}\cdot\boldsymbol{n} = -\frac{M_{H_2O} j A_{active}}{2F\rho_{H_2O}}$$

with the normal vector $\boldsymbol{n}$ of the PTL surface in contact with the anode catalyst layer, the nominal current density j, the Faraday

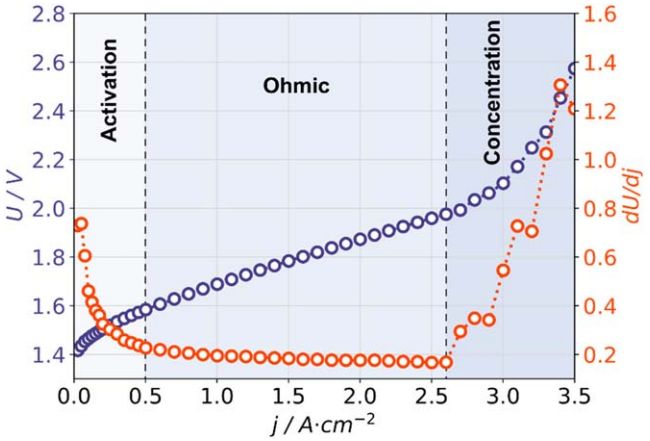


Figure 2. Polarization curve (blue) and derivative dU/dj (orange) for a flow rate of 3 ml min^{-1} with a flow field temperature of 65 °C and a current density up to 3.5 A·cm^{-2}.

constant F, and the molecular weights of oxygen M_{O_2} and water M_{H_2O}, respectively. Lastly, ρ_{O_2} and ρ_{H_2O} denote the densities of oxygen and water, respectively.[20] The circular area of the lower cylinder is defined as the water inlet. A water velocity equivalent to the flow rate of 3 ml min^{-1} is specified. At the outlet (upper cylinder), we assume ambient pressure as BC.

The model for the two-phase flow within the flow field and the (geometric) structure of the flow field is set up in COMSOL Multiphysics®.[39,40] The SI further describes the equation system and the computational model.

Results

Polarization.—Figure 2 shows the recorded polarization curve and its derivative dU/dj, representing the cell resistance. By observing the course of the polarization curve, the three characteristic regimes activation polarization, ohmic polarization -subdivided into quasi ohmic and true ohmic regime- and concentration polarization can be identified. Starting at a low current density of 0.005 A·cm^{-2}, there is a progressive growth up to a current density of about 0.5 A·cm^{-2}. This range is referred to as activation polarization and is characterized by a strong decrease in the slope (dU/dj), starting at 0.75 Ω and subsequently decreasing to approx. 0.2 Ω up to 0.5 A·cm^{-2}.

In the second range, the ohmic polarization range, extending from 0.5 A·cm^{-2} to 2.6 A·cm^{-2}, from 0.5 to 1.6 A·cm^{-2} the voltage increases with increase in current shows only minor deviation from linearity while from 1.6 to 2.6 A·cm^{-2} the JV-curve is almost linear. The derivative dU/dj of the voltage with respect to current density is around 0.2 Ω. From 2.6 A·cm^{-2} on, a considerable increase in voltage can be observed, marking the third range. This is also reflected in the derivative with an exponential increase from 0.2 to ∼1.3 Ω.

Impedance.—The three different regimes described above—activation polarization, ohmic polarization and concentration polarization—are also reflected in the Nyquist plots shown in Fig. 3. The total impedance (low-frequency intercept) decreases considerably up to a current density of 0.5 A·cm^{-2}, following a slight decrease in the medium current density range (0.5–2.6 A·cm^{-2}). However, the total impedance increases significantly at higher current densities (>2.6 A·cm^{-2}). The impedance spectra are comprised of three distinct resistance contributions: the ohmic resistance (R_0) (Im(Z) = 0 at high frequencies), the intermediate-frequency semicircle (R_1), and the low-frequency semicircle (R_2). An exemplary Nyquist plot at 2.7 A·cm^{-2} in Fig. S12 depicts these resistance contributions mentioned above, obtained by intercepting real-axis of impedance using the model represented in Fig. S4.

Figure 3a shows the Nyquist plots in the activation polarization region for current densities from 0.1 to 0.5 A·cm^{-2}. R_0 remains constant at around 6.1 mΩ for these current densities. The intermediate-frequency semicircle R_1 is much more distinct than the low-frequency semicircle and decreases sharply with increasing current density, whereas the low-frequency semicircle R_2 is not directly visible and can only be surmised, meaning that R_2 is close to zero in this range of current density and only starts to appear around 0.5 A·cm^{-2}.

The Nyquist plots for the ohmic region, subdivided into a quasi-ohmic region, in which the JV-curves deviates only slightly from a linear behavior, and a true-ohmic region, where the JV-curve is almost linear, are shown in Figs. 3b and 3c, respectively. In the quasi-ohmic region for current densities from 0.5 to 1.6 A·cm^{-2}, the spectra show a similar trend as in the activation polarization region, with the intermediate-frequency semicircle R_1 decreasing to a lesser degree compared to the activation polarization region. The ohmic resistance R_0 decreases very slightly with increasing current density, however this change can be considered negligible. The low-frequency semicircle R_2 is still very small, but clearly identifiable and increases slightly with increasing current density. In the ohmic region from 1.6 to 2.6 A·cm^{-2}, the Nyquist plots in Fig. 3c show no significant changes.

For current densities >2.6 A·cm^{-2}, the impedance starts to increase again, with a sharp increase in ohmic resistance R_0 and a strong growth of the low-frequency semicircle R_2, while the intermediate-frequency semicircle R_1 shows only a slight increase, as illustrated in the Nyquist plots in Fig. 3d.

A comparison with literature data allows identifying the key characteristic of Nyquist plots for electrochemical systems, consisting of an ohmic resistance (high-frequency intercept), an intermediate-frequency semicircle, and a low-frequency semicircle at higher current densities. The ohmic resistance R_0 is consistently interpreted as the resistances of electrical and ionic conductive elements. Interpretations of the low- and intermediate-frequency semicircle in literature differ, however.[28,32,41–43] The intermediate-frequency semicircle R_1 may originate from (low) cathodic catalyst loadings leading to an increase in resistance due to the hydrogen evolution reaction (HER), while the low-frequency semicircle R_2 is often assigned to the charge transfer resistance during OER.[41] In other studies, the intermediate-frequency semicircle R_1 is interpreted as being caused by charge transfer losses during OER while the low-frequency semicircle R_2 may be caused by sluggish transport kinetics in PTLs.[28,32,42–44] With low water flow rates in a PEMEC system, the low-frequency semicircle can also be attributed to mass transfer resistance.[28] Investigations using a segmented single-channel PEMEC showed a partial low-frequency semicircle at higher current densities with low water flow rates (stoichiometric ratio $\lambda > 4$), particularly at the outlet. The formation of this semicircle in the EIS spectra was attributed to mass transport losses caused by replacement of water by bubbles.[32] As the applied flow rates can potentially lead to volume occupied by bubbles at higher current densities and a potential accumulation of oxygen at the catalyst surface, we attribute in our case this low-frequency semicircle to an increase in mass transfer resistance.

Figure 4 illustrates the development of the impedance components over the complete range of current densities. The equivalent circuit model shown in Fig. S4 was utilized to obtain resistances. The ohmic resistance R_0, which as discussed mainly represents the resistance of the membrane, remains almost constant up to 2.7 A·cm^{-2} with only a slight decrease due to minor temperature increases. From 2.8 A·cm^{-2} onward however, a substantial increase in the ohmic resistance can be observed. The charge transfer resistance R_1 connected to the OER decreases up to 1.6 A·cm^{-2}, reaches its minimum there and remains almost constant up to 2.8 A·cm^{-2} from which point on it starts to increase. The mass transfer resistance R_2 can initially be observed starting around 0.5 A·cm^{-2}, increasing slightly up to 2.6 A·cm^{-2}, and then rising significantly with higher current densities. Since these results,

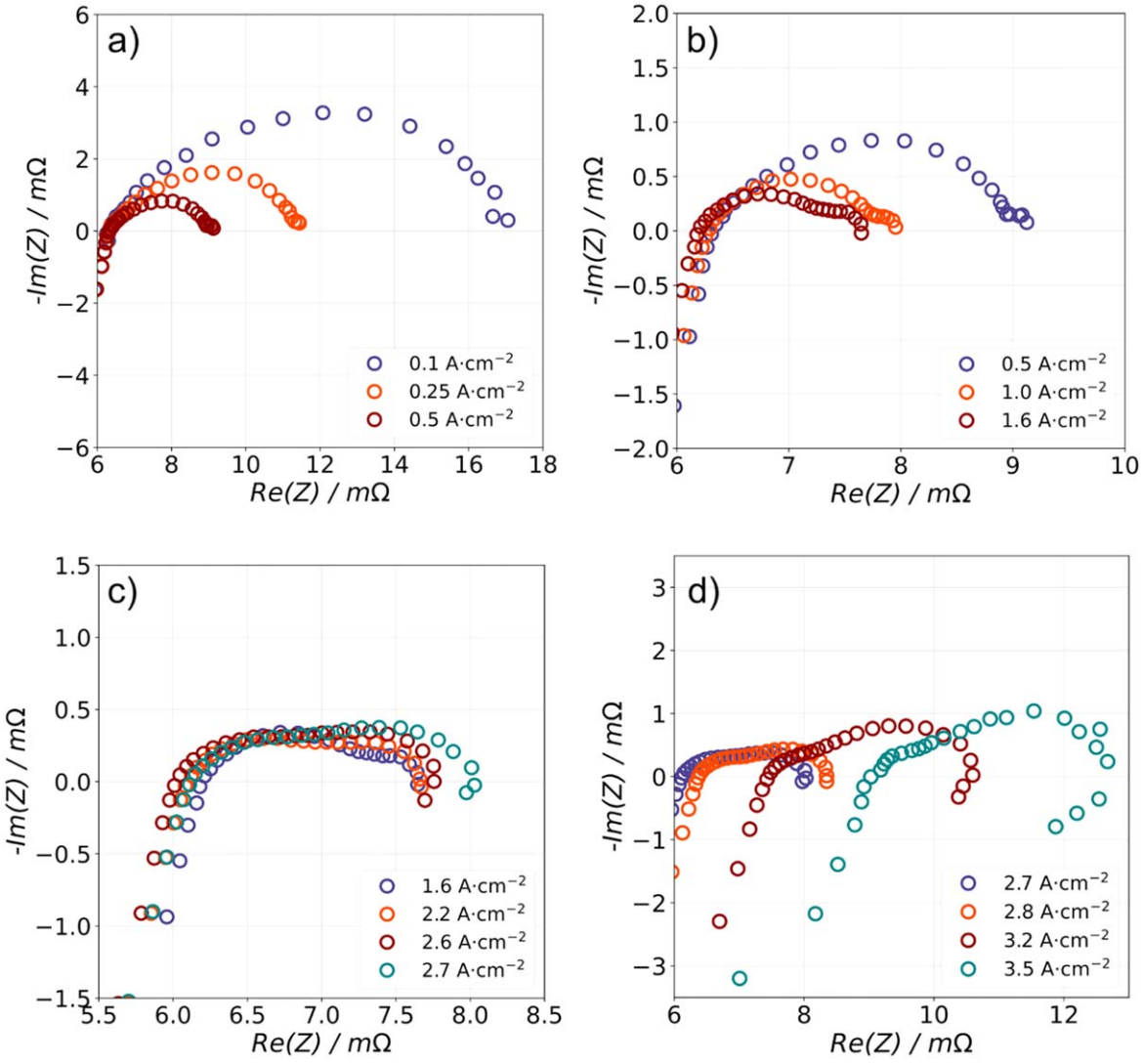


Figure 3. Nyquist plots at different current densities for a flow rate of 3 ml min^{-1} with a flow field temperature of 65 °C. (a) The activation region at low current densities of 0.1, 0.25 and 0.5 A·cm^{-2}; (b) the quasi ohmic region at current densities between 0.5 and 1.6 A·cm^{-2}; (c) the ohmic region with the transition to the concentration region up to current densities of 2.7 A·cm^{-2}; and (d) the concentration region up to current densities of 3.5 A·cm^{-2}.

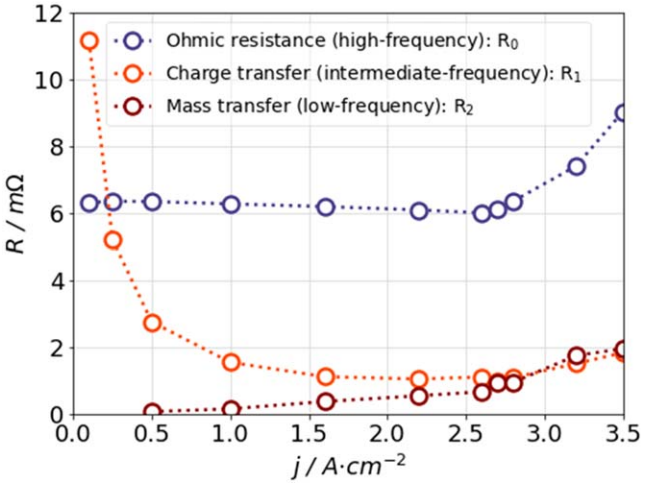


Figure 4. Fitting of the individual resistances over the full range of current densities according to the equivalent circuit model shown in Fig. S4.

especially for R_2, appear to be associated with an increase in gas accumulation at the anode and a potential change in the two-phase flow, they need to be connected to the gas bubble dynamics and coverage at the anode.

Bubble visualization and quantification.— *Description of local flow patterns.*—The bubble coverage is observed using the high-speed camera setup at current densities of 0.2, 2.0 and 2.8 A·cm^{-2} as representative values for the activation polarization, ohmic polarization and concentration polarization regimes, shown in Fig. 5. In the regions of the channel filled exclusively with water, the channel walls and the PTLs are clearly recognizable. At 0.2 A·cm^{-2} and 2.0 A·cm^{-2}, two types of bubbles can be distinguished. Small gas bubbles can be recognized as darker circles that distort the appearance of the PTL. When the small gas bubbles coalesce into larger bubbles filling the entire width of the channel, the bubbles appear brighter than the liquid phase. In these regions, the PTL remains visible, but less clear than with a pure liquid phase. These two types of bubbles, small, isolated bubbles and large coalesced bubbles can be identified by the applied image processing algorithm. Overall, both bubbly flow and slug flow can be observed. At current

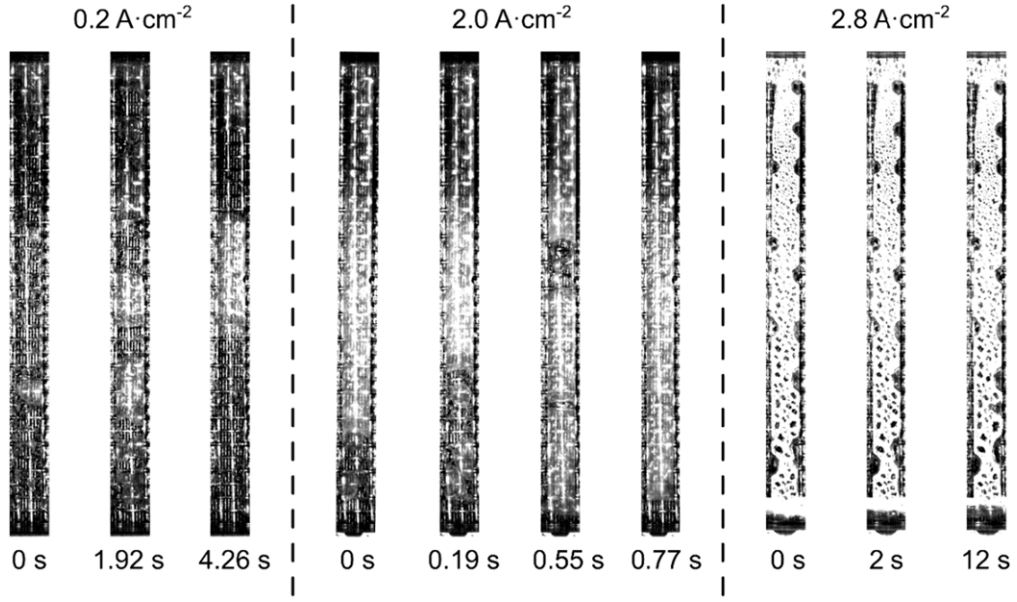


Figure 5. Two-phase flow in a typical channel of the anode side flow field with a flow rate of 3 ml min^{-1} and a flow field temperature of 65 °C in the activation region at 0.2 A·cm^{-2}, the ohmic region at 2 A·cm^{-2} and the concentration region at 2.8 A·cm^{-2}.

densities higher than 2.8 A·cm^{-2} the characteristics of the flow change significantly where only the channel surface covered by condensed droplets can be observed. The flow from spots free of condensate and the presence of the condensate indicate a mainly coherent gas flow instead of a two-phase flow with individual gas bubbles in the liquid. In this regime the flow conditions are not accessible to image processing.

In a time-dependent observation of the evolution of the flow at 0.2 A·cm^{-2}, small gas bubbles form over the entire length of the channel, mainly on the left and right edges of the channel at the beginning of the measurement period at 0 s. The gas bubbles then continue to grow and finally coalesce with the neighboring bubbles. After 1.92 s, three larger bubbles can be seen in the same channel, which now fill the entire width of the channel. The gas bubbles continue to grow, remain stagnant and finally detach to flow through the channel from bottom to top. In the image at 4.26 s, the lower bubble previously observed at 1.92 s can be seen, has now grown and has already detached and is flowing through the channel from bottom to top. New small bubbles are already visible in the lower part of the channel, forming on the left and right, starting the process all over again.

Similar processes are observed at 2.0 A·cm^{-2}, however, involving larger bubbles and happening considerably faster. At the beginning of the measurement period at t = 0 s, only in the lower 20%, smaller gas bubbles can be seen forming on the left and right of the channel edge, while the remaining 80% of the channel are filled with large gas bubbles. After 0.19 s, these smaller bubbles coalesce again to form a gas bubble that fills the entire channel. At the same time, the large bubble moves further upwards and has shifted upwards by about 20% of the channel length. In the vacated area, new small gas bubbles form on the left and right channel edges. After 0.55 s, these gas bubbles coalesce again to form a large gas bubble. Coalescence with the lower large bubble, which was stationary up to now, is now imminent. This process continues until the upper gas bubble has completely left the channel. After 0.77 s, the channel is completely filled by a gas bubble again.

The observations described here are consistent with the video data (S13—S15) analyzed using the image-processing algorithm. The average bubble size, shown in Fig. 6, shows an almost linear increase up to 2.0 A·cm^{-2}. Starting at 0.2 A·cm^{-2}, the bubble size is approx. 12.5 mm^2, increasing fourfold to approx. 50 mm^2 at 1 A·cm^{-2} and then triplicate to approx. 140 mm^2 at 2 A·cm^{-2}.

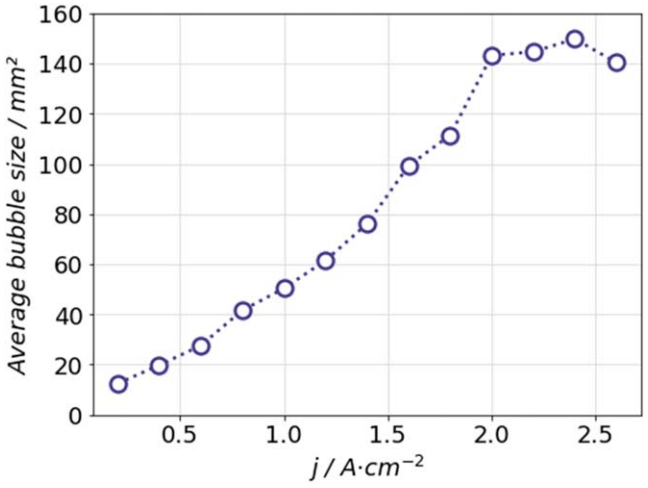


Figure 6. Average bubble size in the anode side flow field with a flow rate of 3 ml min^{-1} and a flow field temperature of 65 °C size as a function of current density.

From here, the bubble size remains roughly constant up to 2.6 A·cm^{-2}.

The images recorded at current densities higher than 2.7 A·cm^{-2} indicate that there is a limited amount of water in the PEMEC at higher current densities, meaning that the channels are predominantly filled with gas. The PEMEC is actively heated to 65 °C and heats further up to 74 °C at high current densities. As a result, the water is no longer present in a majorly liquid form, but predominantly in gaseous form, meaning that the gas phase consists of oxygen and water vapor. As the surface of the flow field is slightly cooler than the PTL, water vapor condenses on the surface and forms fine droplets, leading to increased brightness in the image due to increased reflection of the LED illumination. These results show that at higher current densities (>2.7 A·cm^{-2}), a two-phase flow can no longer be observed but rather only a single-phase gas flow.

Description of gas bubble coverage in the complete flow field.—Figure 7 shows exemplary images from the video recordings at current densities of 0.2, 2.0 and 2.8 A·cm^{-2} characteristic for the

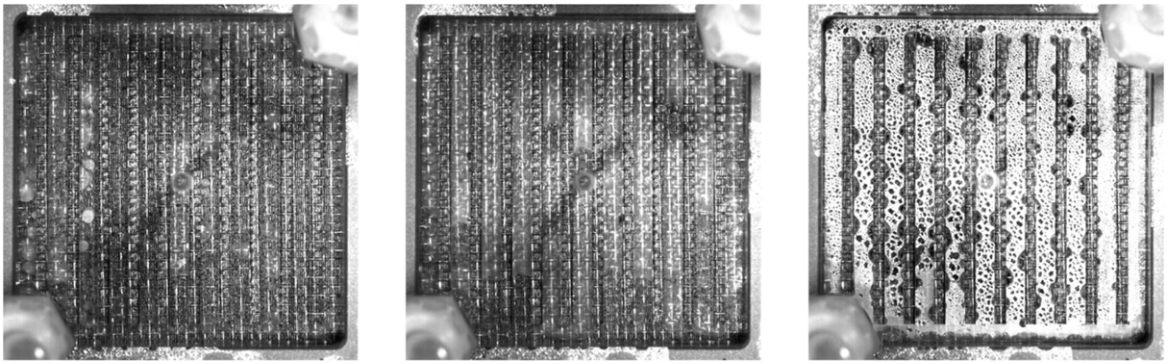


Figure 7. Two-phase flow within the anode side flow field with a flow rate of 3 ml min^{-1} and a flow field temperature of 65 °C in the activation region at 0.2 $A{\cdot}cm^{-2}$, the ohmic region at 2 $A{\cdot}cm^{-2}$ and the concentration region at 2.8 $A{\cdot}cm^{-2}$.

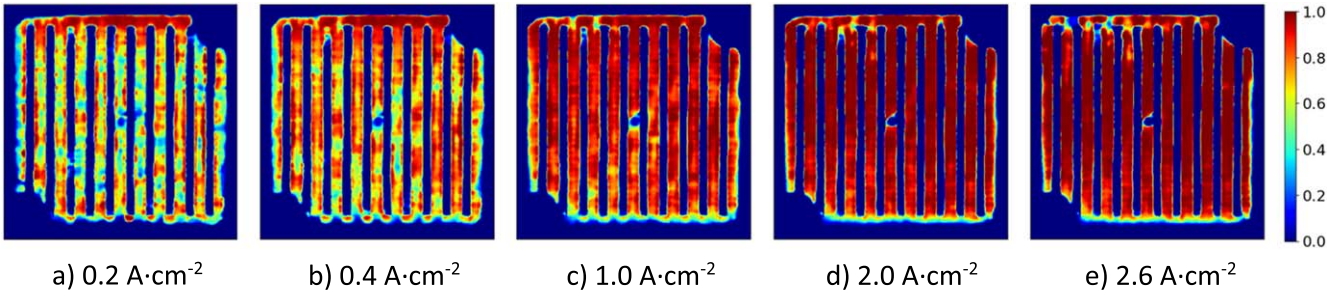


Figure 8. Experimental frequency distributions of the bubbles inside the anode side flow field for different current densities with a flow rate of 3 ml min^{-1} and a flow field temperature of 65 °C from the high-speed video recordings using the image processing algorithm.

flow patterns in the activation polarization, the ohmic and the high current regimes.

In the activation and the ohmic region, a two-phase flow regime is observable in the entire flow field (Figs. 7a and 7b). Gas bubbles grow in the liquid phase up to the width of the channel and flow through the channel from bottom to top. A comparison of 0.2 $A{\cdot}cm^{-2}$ and 2.0 $A{\cdot}cm^{-2}$ indicates that at 2.0 $A{\cdot}cm^{-2}$ the channels are filled with oxygen bubbles to a much larger degree. This pattern continues up to 2.6 $A{\cdot}cm^{-2}$ and changes significantly above higher current densities. At these high current densities, the surface of the entire flow field, apart from the lower horizontal distribution channel, is covered with the previously described brightly illuminated condensation film. Observations through semi-transparent spots show mainly gas flow with few scattered sections of liquid containing small bubbles on the PTL surface. This observation and the appearance of the condensation film indicate that large part of the vertical channels and the upper horizontal collection channel are predominantly covered by a coherent gas flow. Since the algorithm is built up and trained for detecting bubbles in a two-phase flow, it cannot be applied for the analysis of the changed flow pattern in the high current density region since it more closely represents a one-phase gaseous flow. The typical two-phase flow, which occurs at lower current densities, can only be recognized in the lower horizontal channel.

Quantification of the experimentally determined frequency distribution of gas bubbles in the flow field.—Quantification of the gas coverage and the spatial distribution of the gas bubbles within the flow field illustrated by the frequency distributions of the gas bubbles, is shown in Fig. 8. The bubble coverage distributions in the flow field were determined by recording a total of 2670 images within 12 s, 5 s after starting the run at each current density. The image processing algorithm superimposes all the individual images and calculates the frequency of bubbles and the overall gas coverage of the flow field occurring at each point.

At a current density of 0.2 $A{\cdot}cm^{-2}$, the flow field is about 55% filled with gas (Fig. 8a). The lower horizontal channel, which distributes the inflow (from the lower left corner) to the 11 vertical channels, is least filled with gas. In the vertical channels, the gas coverage is mostly between 30% and 70% and even approaching 80% at certain select spots. The upper horizontal channel, which collects the flow from the vertical channels, has an increased gas occurrence of 95% due to gravity and flow direction -At 0.4 $A{\cdot}cm^{-2}$, the region with high gas coverage, which was previously isolated to the upper collection channel, extends further toward the upper third of the vertical channels (Fig. 8b). In general, the amount of gas in the vertical channels is increased compared to 0.2 $A{\cdot}cm^{-2}$, and the distributed select spots with a higher gas amount are larger. The lower horizontal distribution channel shows no significant changes and has the lowest gas content. In total the flow field is about 63% filled with gas.

As the current density increases, the overall proportion of gas in the entire flow field also increases, with a gas proportion of 95% being reached in the upper area of the channels. However, the flow in the lower horizontal inlet distribution channel still shows little to no change and remains at a constant low gas content of around 20% across all current densities. From 2.0 $A{\cdot}cm^{-2}$, areas with a gas content of 90% dominate in all vertical channels (Fig. 8d). This state remains almost unchanged up to 2.6 $A{\cdot}cm^{-2}$; the frequency distributions show only miniscule differences (Fig. 8e). At further increased current densities quantitative evaluation is no longer possible, due to changes in the flow regime.

Modeling distribution of gas content.—Following the measurement procedure in Fig. S3, the gas distribution in the flow field was calculated using a transient two-phase flow mixture model, starting

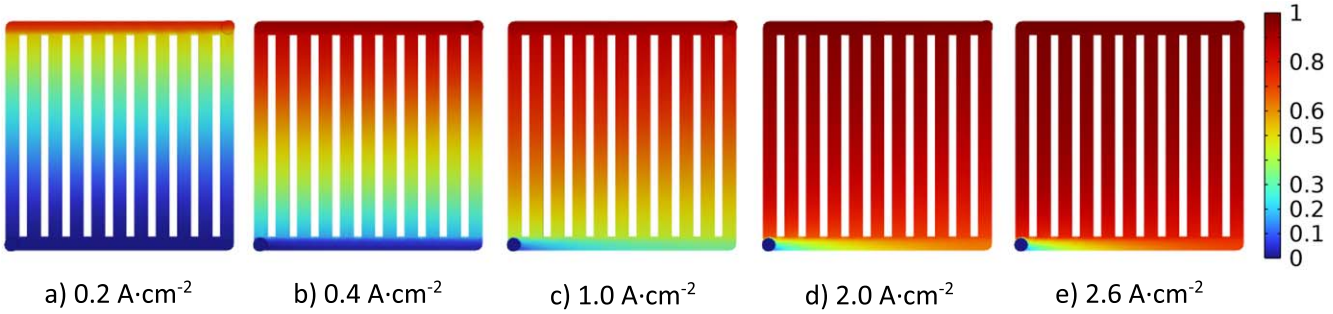


Figure 9. Modeled frequency distributions of the bubbles inside the anode side flow field for different current densities with a flow rate of 3 ml min^{-1} and a flow field temperature of 65 °C with the two-phase flow mixture model.

at t = 0 s with a current density of 0.005 A·cm^{-2}, and the flow field 100% filled with water. For the 0.005 A·cm^{-2} case, the simulation is run for 300 s, whereas for the rest of the current densities the previous simulation is restarted and run for only 17 s. The frequency distributions shown in Fig. 9 represent the time-averaged gas distribution between 5 s and 17 s in the flow field plane closest to the upper channel surface. With the used mixture model, it is not possible to track and map the surfaces of the individual bubbles. Instead, an average value of the gas content in each segment is calculated for each point in the flow field.

At 0.2 A·cm^{-2}, the upper horizontal collection channel has the largest amount of gas with 60%, as in the experimental results (Fig. 9a). The amount of gas decreases towards the bottom, reaching a minimum of approximately 10% in the lower horizontal distribution channel. If the current density is increased to 0.4 A·cm^{-2}, the region with a high gas content spreads from top to bottom, resulting in the upper third of the flow field being 60–80% filled with gas (Fig. 9b). If the current density is further increased to 1.0 A·cm^{-2}, the amount of gas in the lower horizontal distribution channel increases further to approx. 60% (Fig. 9c). The region with a high gas content continues to spread from top to bottom, so that the vertical channels are approximately 80% filled with gas. At 2.0 A·cm^{-2}, the flow field is now predominantly 90% filled with gas, with the lower horizontal bonding channel having the lowest amount of gas at 70% (Fig. 9d).

Experiment vs modeling.—The general trend of the experimental determination of the bubble coverage (Fig. 8) and the modeling of the gas content in the two-phase flow (Fig. 9) with increasing current density are very similar although the experimental and the modeling approach are different with respect to the absolute quantities. This could be due to several reasons, the first being the chosen time period for the evaluation. In the experimental approach, the image processing algorithm superimposes all the individual images recorded during the 12 s runtime starting 5 s after switching to the respective current density and calculates the frequency of bubbles and the overall gas coverage of the flow field occurring at each pixel. The frequency distributions calculated by the modeling averaged the values in this time slope as well, but the modeling starts at t = 0 s with 100% water inside the flow field, which is not the case in the experiments.

The experimental and modeled results for the gas coverage averaged over the entire flow field are plotted in Fig. 10. At 0.2 A·cm^{-2}, the experimentally determined gas coverage is approx. 55% and reaches its maximum of approx. 80% at 2.0 A·cm^{-2}. This then remains roughly constant up to 2.6 A·cm^{-2}. At 0.2 A·cm^{-2}, the modeling shows a lower average gas coverage of 45% and then increases sharply, so that at 0.4 A·cm^{-2}, it is approximately the same as the experimentally determined gas coverage at 65%. From here, the modeling overestimates the experiment, so that it has a steeper increase in gas coverage and ends up with 93% at 2.6 A·cm^{-2}, while the experiments reach the maximum of 80% gas coverage at 2.0 A·cm^{-2} and remain almost constant up to 2.6 A·cm^{-2}.

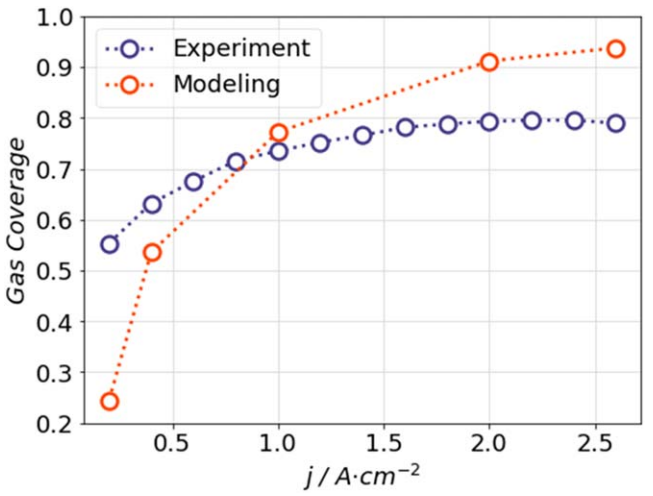


Figure 10. Gas coverage in the anode side flow field with a flow rate of 3 ml min^{-1} and a flow field temperature of 65 °C size as a function of current density evaluated from the high-speed video recordings using the image processing algorithm compared to the modeled data.

The model is able to qualitatively describe the increasing gas fraction with increasing current density and the gradient in gas concentration from inlet to outlet very well as the comparison of Figs. 8 and 9 clearly displays. However, some features that prominently appear in the experimental results cannot be replicated by the utilized modeling approach. For example, the local areas ("hot spots") with a strong increase in gas coverage and the consistently low gas coverage in the horizontal inlet channel and slightly different gas coverage in each vertical channel cannot be properly replicated. Figure S11 shows a change in gas coverage in vertical channels from inlet to outlet for the experimental results which is not observed for the modeling results (Fig. S10). A reason for the discrepancies in the experimental and modeling results could be that the transient two-phase flow mixture model does not consider the impact of electrochemical reactions at the anode (e.g. OER kinetics) or the physical interactions of the gas bubbles with the electrode surface. Furthermore, due to the isothermal nature of the model, the temperature distribution in the cell cannot be fully reflected. These and other influencing factors lead to local inhomogeneities in the gas coverage that in turn lead to the model over- or underestimating the total gas coverage quantitatively.

Correlation bubbles vs JV/EIS.—The polarization curve can be divided into three regimes. In the first regime, the activation polarization regime, the voltage increases progressively up to a current density of 0.5 A·cm^{-2}. In this range, the ohmic resistance remains almost constant, while the charge transfer resistance drops sharply. This is due to the accelerated OER at increased potentials. This process is directly reflected in the captured images showing an

increasing gas coverage as well as a growing average bubble diameter.

In the ohmic polarization regime, which extends in the current density range from 0.5 to 2.6 A·cm^{-2}, the ohmic resistance decreases slightly. The charge transfer resistance continues to decrease and reaches its minimum at 2.2 A·cm^{-2}. Meanwhile, a small low-frequency semicircle appears for the first time at 0.5 A·cm^{-2} and, like the gas coverage and the average bubble diameter, increases continuously with increasing current density. The gas coverage and bubble diameter reach their maximum at 2.0 A·cm^{-2}, where each channel is filled with a large gas bubble.

If the current density of 2.6 A·cm^{-2} is exceeded, there is a rapid increase in voltage and resistances. The charge transfer resistance increases slightly, while the ohmic resistance and the low frequency semicircle increase noticeably. A look at the video recordings shows that the flow form in this regime changes completely. A coherent gas flow with only a few areas of liquid flow can be observed. For current densities above 2.6 A·cm^{-2}, the PEMEC is no longer supplied with enough water at the utilized flow rate of 3 ml min^{-1}. As a result, the proton conductivity of the membrane decreases, as less water molecules are available to diffuse through the membrane carrying protons, which leads to an increase in the ohmic resistance. However, the most substantial influence results from the fact that at such high current densities the reaction rate is limited by the availability of water, which is limited by the applied flow rate. This leads to increased mass transfer losses, as illustrated by the sharp increase in the low-frequency semicircle. This third regime is therefore understood as the concentration polarization regime.

Conclusions

An electrolyzer cell with a transparent parallel flow field was designed to study the gas bubble coverage in the flow field during the electrolysis operation using a high-speed camera. JV-curves along with concomitant measurements of the impedance of the cell, while monitoring at the same time the gas evolution on the anode side by means of a high-speed camera, were recorded in 0.1 A·cm^{-2} steps up to current densities of 3.5 A·cm^{-2} with a water inlet flow rate of 3 ml min^{-1} corresponding to a relatively low stochiometric ratio ($\lambda = 6$ at 3.5 A·cm^{-2}). In order to quantify the gas content in the flow field channels a deep learning-based image processing algorithm was implemented. By means of this the gas coverage was quantified up to 2.6 A·cm^{-2} and compared with calculations of the two-phase flow in the anodic flow field through 3D mixture model with oxygen production and water consumption introduced via boundary conditions. The primary observations of this study include:

- Three regimes in the JV curve were clearly distinguished. The first regime, governed by activation polarization, prevailed for current densities less than 0.5 A·cm^{-2} before turning via a smooth transition to a second, almost linear regime, that extended up to 2.6 A·cm^{-2}. In the third regime, that features elevated current densities above 2.6 A·cm^{-2}, a pronounced increase in the measured voltage is observed, reaching 2.6 V at 3.5 A·cm^{-2}.
- In the first two regimes, analysis of the impedance spectra identified an almost constant ohmic resistance and a charge transfer resistance attributed to the OER. The charge transfer resistance kept decreasing up to 2.6 A·cm^{-2}. At current densities above 2.6 A·cm^{-2} both values were increasing. Most importantly, however, in the high current regime (third regime), an additional semicircle at low frequencies became pronounced in the Nyquist plots which was attributed to concentration polarization resulting from the tightening of water supply and diffusion limitation.
- The video recordings reveal that at low current densities (0.2 A·cm^{-2}), the flow field area covered by gas bubbles is around 55%, with the gas coverage being most pronounced in the collecting channel towards the outlet. Along with increasing current density, the gas coverage extends towards the parallel channel area and the area covered by gas bubbles increases to 80% at 2.0 A·cm^{-2}. This remains roughly constant up to 2.6 A·cm^{-2}. When current densities are higher than 2.6 A·cm^{-2}, the pattern of the gas coverage changes completely. An interconnected gas flow with small areas of liquid in between can be observed instead of a flow pattern with individual bubbles.
- Calculations of the two-phase flow in the anodic flow field up to 2.6 A·cm^{-2} by means of a 3D mixture model with oxygen production and water consumption introduced via boundary conditions showed qualitative agreement with the experimental results on total area gas coverage and gas distribution in the flow field. Both demonstrated an inhomogeneous gas distribution with a gas accumulation towards the upper part of the flow field close to the outlet.
- The profile of the JV curve and the results from the impedance analysis indicate that the onset of the nonlinear concentration polarization regime with strongly increasing voltage in the high current density region and the pronounced appearance of a third resistance component coincide with high area coverage with gas bubbles and a transition to an interconnected gas flow regime.

The inhomogeneous gas distribution was observed with a gas accumulation in the upper part of the flow field close to the outlet, which could become especially relevant in large-scale applications since it might lead to locally increased degradation due to e.g. drying. A simple solution might be to increase the flow rate to higher levels; this however comes with its own drawbacks since this increase in flow rate might lead to degradation effects of its own e.g. damage of the catalyst layer by mechanical removal of particles or stronger membrane thinning. The effect of locally increased gas coverage on long-term stability and the possible detrimental effects of higher flow rates still needs to be studied in order to find the ideal trade-off. All in all, the results at hand clearly demonstrate the importance of considering and analyzing the gas coverage and choosing the correct flow rate when designing and operating efficient and durable PEM electrolysis cells.

Acknowledgments

The authors gratefully acknowledge the financial support by the German Federal Ministry of Education and Research (BMBF) within the H2Giga projects DERIEL (grant number 03HY122C). Many thanks to Tobias Offermanns, Albert Luft and Marcel Turiaux for their support with the cell construction and test rig setup.

ORCID

Fabian Meyer https://orcid.org/0009-0009-3762-2835
Violeta Karyofylli https://orcid.org/0000-0002-7479-3993
André Colliard Granero https://orcid.org/0000-0002-4615-3710
Ali Javed https://orcid.org/0000-0002-9947-0904
Michael Eikerling https://orcid.org/0000-0002-0764-8948
Hans Kungl https://orcid.org/0000-0003-3142-3906
Eva Jodat https://orcid.org/0009-0004-8214-2981
André Karl https://orcid.org/0000-0003-2289-5987
Rüdiger-A. Eichel https://orcid.org/0000-0002-0013-6325

References

1. A. Karl, E. Jodat, H. Kungl, L. Dobrenizki, G. Schmid, and P. Geskes, "Water electrolysis facing the gigawatt challenge—comprehensive De-Risking of proton exchange membrane and anion exchange membrane electrolyser technology." *Electrochemical Science Advances* (Wiley Online Library) (2025).
2. M. Carmo, D. L. Fritz, J. Mergel, and D. Stolten, "A comprehensive review on PEM water electrolysis." *Int. J. Hydrog. Energy.*, **38**, 4901 (2013).
3. J. O. Majasan, J. I. S. Cho, I. Dedigama, D. Tsaoulidis, P. Shearing, and D. J. L. Brett, "Two-phase flow behaviour and performance of polymer electrolyte membrane electrolysers: electrochemical and optical characterisation." *Int. J. Hydrog. Energy.*, **43**, 15659 (2018).
4. R. E. Clarke, S. Giddey, F. T. Ciacchi, S. P. S. Badwal, B. Paul, and J. Andrews, "Direct coupling of an electrolyser to a solar PV system for generating hydrogen." *Int. J. Hydrog. Energy. März*, **34**, 2531 (2009).
5. F. Barbir, "PEM electrolysis for production of hydrogen from renewable energy sources." *Sol. Energy*, **78**, 661 (2005).
6. N. Wolf, A. Javed, L. Treutlein, H. Kungl, A. Karl, and E. Jodat, "Tuning proton exchange membrane electrolytic cell performance by conditioning Nafion N115-

Based membrane electrode assemblies." *Electrochem. Sci. Adv.*, **5**, e202400038 (2025).
7. A. Javed, N. L. Wolf, F. Meyer, L. Treutlein, H. Kungl, and A. Karl, "Exploring the state-of-operation of proton exchange membrane electrolyzers." *Int. J. Hydrog. Energy*, **98**, 280 (2025).
8. C. Lee, J. Hinebaugh, R. Banerjee, S. Chevalier, R. Abouatallah, and R. Wang, "Influence of limiting throat and flow regime on oxygen bubble saturation of polymer electrolyte membrane electrolyzer porous transport layers." *Int. J. Hydrog. Energy.*, **42**, 2724 (2017).
9. X. Zhao, H. Ren, and L. Luo, "Gas bubbles in electrochemical gas evolution reactions." *Langmuir*, **35**, 5392 (2019).
10. O. F. Selamet, U. Pasaogullari, D. Spernjak, D. S. Hussey, D. L. Jacobson, and M. D. Mat, "Two-phase flow in a proton exchange membrane electrolyzer visualized in situ by simultaneous neutron radiography and optical imaging." *Int. J. Hydrog. Energy. Mai*, **38**, 5823 (2013).
11. S. Yuan, C. Zhao, X. Cai, L. An, S. Shen, and X. Yan, "Bubble evolution and transport in PEM water electrolysis: Mechanism, impact, and management." *Prog. Energy Combust. Sci.*, **96**, 101075 (2023).
12. A. J. Shih, M. C. O. Monteiro, F. Dattila, D. Pavesi, M. Philips, and A. H. M. Da Silva, "Water electrolysis." *Nat. Rev. Methods Primer.*, **2**, 84 (2022).
13. M. Chatenet, B. G. Pollet, D. R. Dekel, F. Dionigi, J. Deseure, and P. Millet, "Water electrolysis: from textbook knowledge to the latest scientific strategies and industrial developments." *Chem. Soc. Rev.*, **51**, 4583 (2022).
14. F. Yang, M. Jun Kim, M. Brown, and B. J. Wiley, "Alkaline water electrolysis at 25 A cm−2 with a microfibrous flow-through electrode." *Adv. Energy Mater.*, **10**, 2001174 (2020).
15. C. V. Pham, D. Escalera-López, K. Mayrhofer, S. Cherevko, and S. Thiele, "Essentials of high performance water electrolyzers—from catalyst layer materials to electrode engineering." *Adv. Energy Mater.*, **11**, 2101998 (2021).
16. A. Angulo, P. Van Der Linde, H. Gardeniers, M. Modestino, Fernández, and D. Rivas, "Influence of bubbles on the energy conversion efficiency of electrochemical reactors." *Joule. März*, **4**, 555 (2020).
17. Y. Li, G. Yang, S. Yu, J. Mo, K. Li, and Z. Xie, "High-speed characterization of two-phase flow and bubble dynamics in titanium felt porous media for hydrogen production." *Electrochimica Acta. Februar*, **370**, 137751 (2021).
18. M. Maier, Q. Meyer, J. Majasan, R. E. Owen, J. B. Robinson, and J. Dodwell, "Diagnosing stagnant gas bubbles in a polymer electrolyte membrane water electrolyser using acoustic emission." *Front Energy Res.*, **8**, 582919 (2020).
19. I. Sinapan, C. Lin-Kwong-Chon, C. Damour, J. J. Amangoua Kadjo, and M. Benne, "Revealing anodic multi-class bubble dynamics in PEMWE systems using deep learning and post-processing detection." *Fuel. Mai*, **364**, 131112 (2024).
20. J. C. Garcia-Navarro, M. Schulze, and K. A. Friedrich, "Detecting and modeling oxygen bubble evolution and detachment in proton exchange membrane water electrolyzers." *Int. J. Hydrog. Energy*, **44**, 27190 (2019).
21. W. Wang, S. Yu, K. Li, L. Ding, Z. Xie, and Y. Li, "Insights into the rapid two-phase transport dynamics in different structured porous transport layers of water electrolyzers through high-speed visualization." *J. Power Sources*, **516**, 230641 (2021).
22. H. Zhou, K. Meng, W. Chen, and B. Chen, "Two-phase flow evolution and bubble transport characteristics in flow field of proton exchange membrane water electrolyzer based on volume of fluid-coupled electrochemical method." *J. Clean. Prod.*, **425**, 138988 (2023).
23. Y. Xu, G. Zhang, L. Wu, Z. Bao, B. Zu, and K. Jiao, "A 3-D multiphase model of proton exchange membrane electrolyzer based on open-source CFD." *Digit Chem. Eng. Dezember*, **1**, 100004 (2021).
24. K. H. Rho, Y. Na, T. Ha, and D. K. Kim, "Performance analysis of polymer electrolyte membrane water electrolyzer using OpenFOAM®: two-phase flow regime." *Electrochemical Model. Membranes.*, **10**, 441 (2020).
25. D. Zhu, L. Xu, X. Su, B. Hu, T. Jia, and L. Mi, "Experimental study of the effect of mechanical vibration and water velocity on bubble management in PEM electrolysis cell." *Int. J. Hydrog. Energy*, **49**, 390 (2024).
26. S. Xin, X. LiJun, Z. Di, H. Bing, and M. LuXiang, "Electrochemical performance study of proton exchange membrane electrolyzer considering the effect of bubble coverage." *Int. J. Hydrog. Energy*, **48**, 27079 (2023).
27. Y. Li, Z. Kang, J. Mo, G. Yang, S. Yu, and D. A. Talley, "In-situ investigation of bubble dynamics and two-phase flow in proton exchange membrane electrolyzer cells." *Int. J. Hydrog. Energy*, **43**, 11223 (2018).
28. I. Dedigama, P. Angeli, K. Ayers, J. B. Robinson, P. R. Shearing, and D. Tsaoulidis, "In situ diagnostic techniques for characterisation of polymer electrolyte membrane water electrolysers—Flow visualisation and electrochemical impedance spectroscopy." *Int. J. Hydrog. Energy. März*, **39**, 4468 (2014).
29. H. Ito, T. Maeda, A. Nakano, Y. Hasegawa, N. Yokoi, and C. M. Hwang, "Effect of flow regime of circulating water on a proton exchange membrane electrolyzer." *Int. J. Hydrog. Energy*, **35**, 9550 (2010).
30. N. Shao, A. Gavriilidis, and P. Angeli, "Flow regimes for adiabatic gas–liquid flow in microchannels." *Chem. Eng. Sci. Juni*, **64**, 2749 (2009).
31. S. Sun, Y. Xiao, D. Liang, Z. Shao, H. Yu, and M. Hou, "Behaviors of a proton exchange membrane electrolyzer under water starvation." *RSC Adv.*, **5**, 14506 (2015).
32. C. Immerz, B. Bensmann, P. Trinke, M. Suermann, and R. Hanke-Rauschenbach, "Local current density and electrochemical impedance measurements within 50 cm single-channel PEM electrolysis cell." *J. Electrochem. Soc.*, **165**, F1292 (2018).
33. A. Colliard-Granero, K. A. Gompou, C. Rodenbücher, K. Malek, M. H. Eikerling, and M. J. Eslamibidgoli, "Deep learning-enhanced characterization of bubble dynamics in proton exchange membrane water electrolyzers." *Phys. Chem. Chem. Phys.*, **26**, 14529 (2024).
34. O. Ronneberger, P. Fischer, and T. Brox, "U-Net: convolutional networks for biomedical image segmentation." *arXiv*, **-**, – (2015), 10.48550/arXiv.1505.04597.
35. S. Xie, R. Girshick, P. Dollar, Z. Tu, and K. He, "Aggregated residual transformations for deep neural networks." *IEEE Conference on Computer Vision and Pattern Recognition (CVPR)* (IEEE, Honolulu, HI) (2017), [zitiert 2. Dezember 2024]. S. 5987–95. Verfügbar unter: http://ieeexplore.ieee.org/document/8100117/.
36. J. Deng, W. Dong, R. Socher, L. J. Li, L. Kai, and F.-F. Li, "ImageNet: a large-scale hierarchical image database." *IEEE Conference on Computer Vision and Pattern Recognition* (IEEE, Miami, FL) (2009), [zitiert 2. Dezember 2024]. S. 248–55. Verfügbar unter: https://ieeexplore.ieee.org/document/5206848/.
37. R. Tkachenko, I. Izonin, N. Kryvinska, I. Dronyuk, and K. Zub, "An approach towards increasing prediction accuracy for the recovery of missing IoT data based on the GRNN-SGTM ensemble." *Sensors*, **20**, 2625 (2020).
38. M. Andersson, S. B. Beale, M. Espinoza, Z. Wu, and W. Lehnert, "A review of cell-scale multiphase flow modeling, including water management, in polymer electrolyte fuel cells." *Appl. Energy*, **180**, 757 (2016).
39. J. Nie and Y. Chen, "Numerical modeling of three-dimensional two-phase gas–liquid flow in the flow field plate of a PEM electrolysis cell." *Int. J. Hydrog. Energy*, **35**, 3183 (2010).
40. COMSOL Multiphysics v. 6.2. Stockholm, Schweden: COMSOL AB; (30.07.2025), www.comsol.com.
41. S. Siracusano, S. Trocino, N. Briguglio, V. Baglio, and A. Aricò, "Electrochemical impedance spectroscopy as a diagnostic tool in polymer electrolyte membrane electrolysis." *Materials*, **11**, 1368 (2018).
42. J. O. Majasan, F. Iacoviello, J. I. S. Cho, M. Maier, X. Lu, and T. P. Neville, "Correlative study of microstructure and performance for porous transport layers in polymer electrolyte membrane water electrolysers by X-ray computed tomography and electrochemical characterization." *Int. J. Hydrog. Energy*, **44**, 19519 (2019).
43. P. Lettenmeier, R. Wang, R. Abouatallah, S. Helmly, T. Morawietz, and R. Hiesgen, "Durable membrane electrode assemblies for proton exchange membrane electrolyzer systems operating at high current densities." *Electrochim. Acta*, **210**, 502 (2016).
44. V. Karyofylli, Y. Danner, K. Ashoke Raman, H. Kungl, A. Karl, and E. Jodat, "Sensitivity analysis and uncertainty quantification in predictive modeling of proton-exchange membrane electrolytic cells." *J. Power Sources*, **600**, 234209 (2024).